Structure and magnetic properties of curved graphene networks and the effects of bromine and potassium adsorption

Kazuyuki Takai,* Tsuyoshi Suzuki, and Toshiaki Enoki
Department of Chemistry, Tokyo Institute of Technology, Ookayama, Meguro, Tokyo 152-8551, Japan

Hirotomo Nishihara and Takashi Kyotani
Institute of Multidisciplinary Research for Advanced Materials, Tohoku University, Aoba-ku, Sendai, Miyagi 980-8577, Japan
(Received 2 March 2010; revised manuscript received 26 March 2010; published 12 May 2010)

The structure and magnetic properties of nanoporous zeolite-templated carbon (ZTC) and its guest-adsorbed systems are investigated using potassium and bromine as guest species. In ZTC, nanopores formed by a three-dimensional curved-graphene network, whose structure is transcribed from the zeolite nanopore structure, are regularly arranged (periodicity: 1.4 nm). The regularity of the nanopore structure is preserved during vacuum heat treatment (<380 °C) and potassium adsorption, though it is destroyed by bromine adsorption. The pristine ZTC has localized spins, whose origin is attributed to those created in the region having a negative curvature in the graphene network, as well as to the contribution of an edge state. The spin concentration is estimated as 1 spin/nanopore and is independent of the heat-treatment temperature up to 380 °C. In potassium-adsorbed ZTC, potassium atoms forming networked clusters in the nanopores are magnetic and undergo a weak ferromagnetic transition at 24 K. The ZTC spins, which are not directly coupled with the potassium spins through exchange interaction, accurately mirror the magnetic behavior of the potassium spins.

DOI: 10.1103/PhysRevB.81.205420 PACS number(s): 75.75.−c, 81.05.ue, 73.22.−f, 81.07.−b

I. INTRODUCTION

The development of materials by employing nanospaces has recently captured the attention of materials scientists since these materials can be used for creating unconventional electronic and magnetic structures, which cannot be built from bulk systems.[1–4] Here, the structure and electronic functions of the nanospace, which plays the role of a host, contribute to the development of unconventional electronic and magnetic nanostructures in the guest species that are accommodated in the nanospace.

Among the nanospace-based architectures, graphene-based materials are known to be one of the most interesting and important host systems that provide nanospaces. In particular, graphite intercalation compounds have been intensively investigated; in these compounds, a variety of guest molecules and atoms intercalated in the two-dimensional (2D) space between graphene sheets form nanostructures having electronic and magnetic functions different from those in the existing bulk materials.[5] Here, charge-transfer interaction between the amphoteric graphene-based host having π electrons and guest intercalates governs the creation of the nanostructures.

Nanoporous carbon such as activated carbon fibers (ACFs) composed of a three-dimensional (3D) disordered network of nanographene sheets is another useful graphene-based host material that shares some common features with graphite, while some features are dissimilar to those in graphite.[6–12] The difference between the features of graphite and nanographene is caused by the lack of regularity and the presence of an open edge in its structure. The irregular structure is a disadvantage in materials design, while the presence of an edge gives the graphene-based host structural and electronic features that are otherwise not generally observed. Indeed, because of the difference in the chemical activities between the edge and the surface of nanographene sheets, guest molecules are assembled in a unique manner.[12] In particular, what is most interesting is the contribution of edges to the magnetic functions in graphene. According to previous studies,[13–15] the edges created by cutting a graphene sheet generate a strongly spin-polarized nonbonding π state (edge state), where edges having magnetic moments participate in causing magnetic interaction between guests and the magnetic nanographene host.

Meanwhile, beginning from an early stage of research on template-based material design, zeolite has been popularly used as a template material with regularly arranged nanospaces. Interestingly, unconventional magnetic properties such as ferromagnetism have been known to result from adsorption of an alkaline metal into the zeolite nanopore, even though the guest alkaline metal and the ingredients of zeolite consist of nonmagnetic elements.[16] Here, the alkaline metal atoms confined in the nanospace form a "supercrystal" consisting of "superatoms" (clusters of alkaline atom adsorbates). Each *s* electron of alkaline metal atoms occupies the electronic states of the superatom, where the electronic structure of the whole system is described as a tight-binding band of "superatoms" with strong electron correlation. In other words, the states in the clusters with well-defined *s* and *p* orbitals act as the basis of the electronic states of the cluster network.[17]

Here, it is natural to reach the idea that the nanospace of zeolite can be utilized as a template to create graphene-based nanostructures having a regular nanospace arrangement. Zeolite-templated carbon (ZTC) prepared by CVD (chemical vapor deposition) is thus an interesting candidate of host nanospace material. Here, the disadvantage resulting from the disordered structure appearing in nanoporous carbon can be overcome. It has a 3D network of graphene sheets that form a periodic surface with negative curvature.[18–20] The

ideal structure of ZTC is roughly a 3D array of fullerenelike cages connected to each other by carbon nanotube channels. In this structure, the cage and the channel correspond to the super-cage and the channel part of the zeolite template, respectively. The presence of pentagons in the hexagonal π-electron network is responsible for the positive curvature at the cage parts, while the presence of higher polygons such as heptagons results in negative curvature at the parts connecting the cage and channel in the ZTC graphene network.

As well as the edge site, the existence of curvature endows graphene with additional functions, and as a result, a new class of graphene-based host materials that have advantage in creating unconventional electronic and magnetic systems can be developed. In the electron systems bound to curved surfaces, as in the curved graphene sheet network, the curvature creates an effective potential.[21] Moreover, according to theoretical calculations,[22,23] the electronic structure of such a network of periodic curved surfaces is basically determined by the way in which the network is constructed by connecting tubes as building blocks. For example, in ZTC, when we use zeolite A as a template, ZTC having a cubic network of connecting tubes is obtained, while the template zeolite Y yields ZTC with a diamond network of tubes. Topologically, the structures of the former and the latter ones are generally called a "*P* surface" and "*D* surface," respectively. By using a different kind of zeolite template, graphene-based nanoporous host materials having various electronic structures can be obtained. This is quite interesting aspect of ZTC from the viewpoint of materials design by exploiting host-guest interactions.

With respect to magnetism, the curvature in the graphene-based network results in another interesting feature. Recent spin density functional calculations for the tetrapod motif composed of a curved graphene sheet,[24] which is considered as the fundamental unit of ZTC with the zeolite Y template, indicate the presence of radical spins at the saddle part having negatively curved graphene surfaces. This magnetic behavior is caused by undercoordinated carbon atoms, which are introduced as a part of higher polygons into the hexagon network and sterically stabilized by the *p* orbital of the surrounding sp^2 carbon atoms. Here, the presence of the curvature causes the mixing in the electronic states between π and σ state in the graphene sheet of ZTC, resulting in the formation of an energy gap in its electronic structure. The presence of the energy gap in the host material leads to a mismatch between the electronic states of the metallic guest species in terms of the energy scale; this reduces the interactions between the curved graphene host and the guest material. Similar to the case of the edge state in the nanographene host, the radial spins produced by the presence of the negatively curved graphene generate the localized spin magnetism in the ZTC nanoporous host.

In reality, the zeolite-templated nanopore space is not completely covered by carbon; rather, it has a large number of open edges of graphene.[25] Therefore, the actual microscopic structure of the ZTC sample has the regular array of cuplike curved graphene sheets connected by thinner cullislike graphene channels, as schematically shown in Fig. 1. Moreover, the periphery site of graphene is occupied by various kinds of functional groups having oxygen as the major component. Thus, both the edge part of the cuplike curved graphene and the cullislike graphene can contribute significantly to the magnetic and electronic properties of actual ZTC sample. In addition to the radical spin accompanied by the negatively curved graphene, it is natural that the edge-state spin has a role to play in the localized spin magnetism of ZTC. Recently, an experimental study on the magnetic properties of actual ZTC samples has indicated ferromagnetic behavior of ZTC prepared by the furfuryl alcohol impregnation and propylene CVD.[26] However, few details have been provided on the experimental procedure, such as pretreatment process and the correlation between the magnetism and structure.

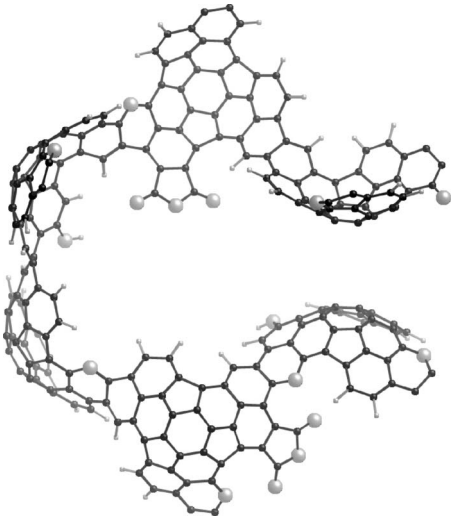

FIG. 1. Schematic view of the microscopic structure of ZTC, where all carbon atoms denoted as small dark gray-colored spheres have threefold coordination (sp^2-carbon). Larger pale gray spheres and small pale gray spheres represent minor oxygen and hydrogen atoms, respectively, which are bonded to the peripheral sites of a curved graphene cage.

In this study, the magnetic properties of ZTC as a network of curved graphene surfaces with a *D* surface topology were investigated in terms of the host-guest interaction with potassium and bromine by measuring magnetic susceptibility and observing electron spin resonance (ESR); here, the effects of pretreatment and the guest adsorption on the structure of ZTC were examined by thermal desorption spectroscopy (TDS), Raman spectroscopy, and x-ray diffraction (XRD).

II. EXPERIMENTAL

Zeolite templated carbon was prepared by acetylene CVD (5% acetylene in N_2) with powdered zeolite Y ($SiO_2/Al_2O_3=5.6$) at 600 °C for 4 h. Then, heat-treatment at 900 °C for 3 h in N_2 and subsequent HF washing were performed in order to remove the zeolite template. Details on the preparation method of ZTC and their characterization are given elsewhere.[25,27,28]

Prior to the guest adsorption and electronic/magnetic measurements, the ZTC sample was evacuated at 1

$\times 10^{-6}$ Torr at room temperature and 200–780 °C for 10 h in order to remove contaminants adsorbed in the nanopores; then, the sample was vacuum-sealed in a Pyrex glass tube. Hereafter, the as-prepared sample and the samples preheat-treated at XXX °C are denoted as non-HT and HTTXXX, respectively. Guest adsorption was performed by using the ZTC sample that was subjected to preheat-treatment at 380 °C in vacuum (HTT380). This sample was referred to as "nonadsorbed ZTC" with respect to the guest adsorbed ZTC. Potassium and bromine were absorbed in Pyrex tubes by the vapor transfer method at 200 °C for 72 h and room temperature for 1 h, respectively; here, bromine was purified by the freeze-pump-thaw method prior to adsorption. Because of the limited amount of the as-prepared ZTC sample available, both the potassium content and bromine content could not be experimentally determined. In order to examine the effect of oxygen contamination on the magnetic measurements, oxygen-adsorbed samples were prepared by the direct introduction of oxygen gas from a high-pressure cylinder to the nonadsorbed ZTC at room temperature. Hereafter, potassium, bromine, and oxygen-adsorbed ZTC are denoted as K-ZTC, Br- ZTC, and O_2-ZTC (YYY Torr), respectively, where YYY is the pressure of the introduced oxygen gas in units of Torr.

TDS spectra were measured by using a Spectra Microvision quadrapole-type mass spectrometer in the temperature range up to 380 °C, with a temperature elevation rate of 5 °C/min. Raman spectroscopy measurements were performed using Jobin-Yvon T64000 instruments with an argon-ion laser operated at 514.5 nm (output power: 10–30 mW) in the backscattering geometry. XRD profiles were measured by Rigaku Ultra X18 with an imaging plate detector that was calibrated using polycrystalline silicon. A Cu Kα target with a graphite monochromator was used as the X-ray source. Magnetic susceptibility measurements were carried out using a SQUID magnetometer (Quantum Design MPMS5) under a field strength of 1 T between 2 and 300 K, where approximately 20 mg of the samples that were vacuum-sealed in Pyrex tubes was used. At 2 and 300 K, the magnetization measurements were also performed at field strengths up to 5.5 T. ESR spectra were measured using an ESR X-band spectrometer (JEOL JES–TE200) at a microwave power of 1 mW in the temperature range 4–280 K for samples with a typical weight of 1 mg; the samples were sealed in a quartz sample tube.

III. RESULTS

The TDS spectra for ZTC (non-HT) exhibit only three peaks, at mass numbers of 18, 28, and 44; these peaks correspond to the chemical species H_2O, CO, and CO_2, respectively, over the entire range of measurement temperatures. Figure 2 shows the TDS spectra for the ZTC (non-HT) sample. The H_2O signal intensity starts to increase rapidly around 80 °C, and further increases above 200 °C. The H_2O peak at 80 °C is correctly attributed to the physisorbed H_2O species in the nanopores of ZTC. The magnitude of the peak becomes high above the temperature corresponding to its bulk boiling point. This suggests that H_2O is weakly bound

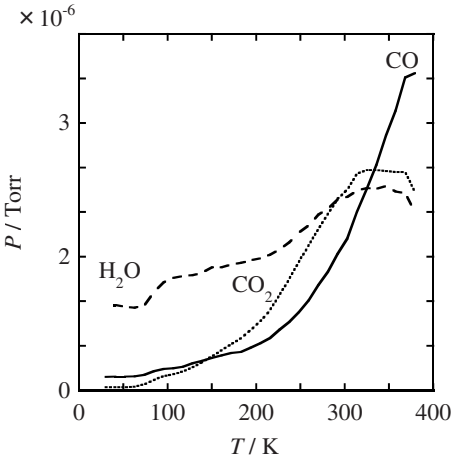

FIG. 2. TDS spectra for the ZTC (non-HT) sample. The solid, dotted, and dashed lines represent the peak intensities for CO, CO_2, and H_2O, respectively. The vertical axis is defined by the partial pressure of each species.

to the polar functional group sites in the nanopore. The H_2O signal shows a maximum around 300 °C and starts decreasing above 350 °C. The presence of CO and CO_2 in the desorbed gas indicates not only the desorption of the foreign species but also the thermal decomposition of the thermally unstable oxygen-containing functional groups bonded to the edge parts of the ZTC structure during the vacuum heat-treatment. The signal corresponding to CO_2 suddenly appears around 80 °C in spite of the negligible contribution below this temperature, and it shows a rapid increase in its intensity above 200 °C. The CO signal intensity gradually increases as the temperatures rise above room temperature; the rate of increase with respect to temperature increases sharply above 300 °C. On the basis of the correlation between the temperature at which the mass signal is observed and the species desorbed through the decomposition, as well as information on the elements included in ZTC, the characteristic temperature 80 °C is partly explained by the decomposition of carboxyl groups in addition to the desorption of physisorbed H_2O, while the CO_2 and CO peaks around 200 °C are attributed to the decomposition of carboxylic anhydride groups.[29–31] Above 350 °C, the intensities for both CO_2 and CO start decreasing. In other words, the adsorbed species and unstable functional groups around the edge part in the ZTC samples are almost removed by heat-treatment up to 380 °C under vacuum.

Figure 3 shows the XRD profile for the non-HT, HTT380, K-ZTC, and Br-ZTC samples. The XRD profiles for the non-HT, HTT380, and K-ZTC samples all exhibited a sharp peak around 6.5°, corresponding to a periodicity of 1.4 nm. On the other hand, the XRD profile for Br-ZTC shows almost no features, although the presence of a peak around 6.5° is confirmed for the nonadsorbed ZTC before bromine adsorption. It is worth mentioning that for all the samples, there is no peak around 26°, where the strong (002) peak assigned to the stacking periodicity of the graphene layers appears in graphite.

Figure 4 shows the Raman spectra for the nonadsorbed ZTC vacuum-degassed at 200 °C, 300 °C, 380 °C, and

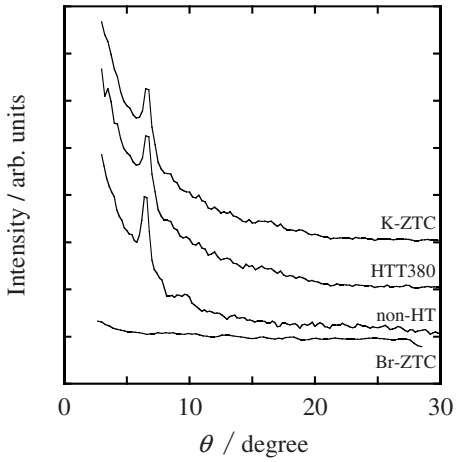

FIG. 3. XRD profiles for the non-HT, HTT380, K-ZTC, and Br-ZTC samples. The vertical axis for each sample is shifted for clarity.

780 °C, as well as for non-HT. As typically observed in materials with a graphitic structure, the *G* band for bending sp^2-bonded carbons and *D* band for breathing aromatic rings are observed around 1600 cm^{-1} and 1350 cm^{-1} for the ZTC samples, respectively. The features of the *G*- and *D*-band peaks are similar, irrespective of the difference in the heat-treatment temperatures for the non-HT, HTT200, HTT300, and HTT380 samples. On the other hand, the line shape for HTT780 is clearly different from that of the others.

The Raman spectra for the guest-adsorbed ZTC samples are shown in Fig. 5, along with those for ZTC380 and ZTC780. In the case of K-ZTC, the line shape is similar to that for HTT380, where the *G*-band peak of the former is shifted toward the low-energy side by 9 cm^{-1}. In contrast to K-ZTC, the spectrum for Br-ZTC is not similar to that for HTT380; rather, it is similar to that for HTT780. The results of Raman spectroscopy for the ZTC samples are summarized in Table I.

Figure 6 shows the temperature-dependence of the magnetic susceptibility χ and the χT value for the non-HT,

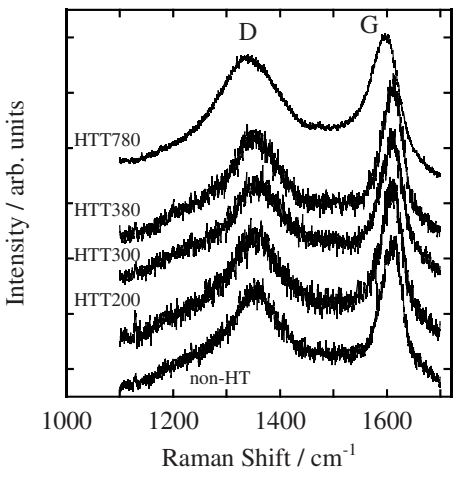

FIG. 4. Raman spectra for nonadsorbed ZTC heat-treated under vacuum at 200 °C, 300 °C, 380 °C, and 780 °C, as well as for non-HT. The vertical axes are shifted for clarity.

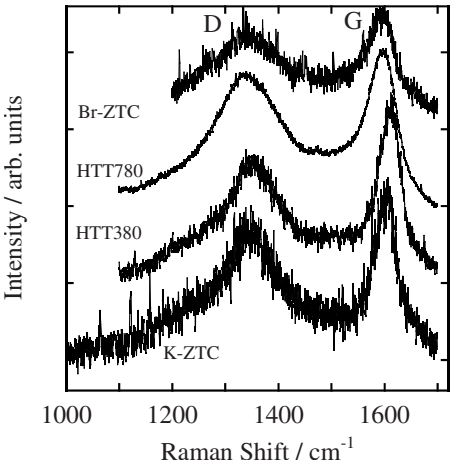

FIG. 5. Raman spectra for nonadsorbed heat-treated ZTC (HTT380, HTT780) and guest adsorbed ZTCs (K-ZTC, Br-ZTC). The vertical axes are shifted for clarity.

HTT200, HTT300, HTT380, and HTT780 samples. All the samples show paramagnetic behavior over the entire range of measurement temperatures (2 K–300 K), with the χT value decreasing below 10 K; further, a temperature-independent diamagnetism term is also present. In the χT plots, humps appear around 80–100 K in the case of the non-HT and HTT200 samples. The temperature-dependence of the χT value is shown for the K-ZTC, Br-ZTC, O_2-ZTC (0.01 Torr), HTT380, and HTT780 samples in Fig. 7. In contrast to the case of HTT380, which is used as a host for potassium doping, a prominent peak appears at 16 K in the χT vs T plots for K-ZTC. The plot of χT for O_2-ZTC (0.01 Torr) also shows a hump; this hump is quite broad and positioned around 100 K, similar to that observed for the non-HT samples (Fig. 7). The Br-ZTC exhibits no feature in the χT vs T plots, which is almost temperature independent in the

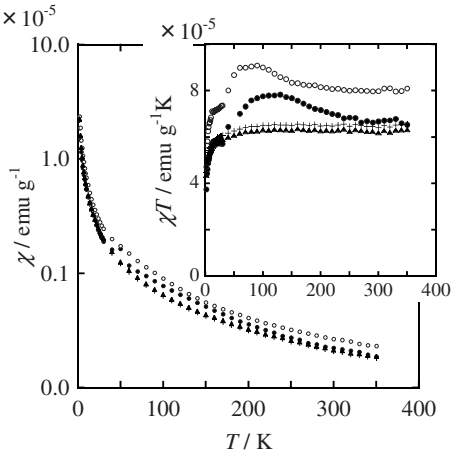

FIG. 6. The temperature-dependence of the magnetic susceptibility χ for non-HT, HTT200, HTT300, and HTT380. The inset shows the temperature-dependence of the χT value for each sample. The solid circles, open circles, crosses, and closed triangles represent non-HT, HTT200, HTT300, and HTT380, respectively. Each datum is obtained after the temperature-independent term is subtracted from the observed susceptibility.

TABLE I. The peak positions and the linewidths of the Raman *G* and *D* band, as well as the crystalline sizes for non-HT, HTT200, HTT300, HTT380, K-ZTC, and Br-ZTC. The Raman peak position and its linewidth are expressed in cm^{-1}, while the crystalline size is expressed in nm.

Sample	*G* position	*G* linewidth	*D* position	*D* linewidth	Crystalline size	I_G/I_D
non-HT	1610	26	1353	80	3	0.46
HTT200	1609	25	1352	87	2	0.43
HTT300	1609	25	1356	85	2	0.44
HTT380	1610	27	1355	75	3	0.47
HTT780	1596	37	1340	75	3	0.56
K-ZTC	1601	25	1345	50	3	0.62
Br-ZTC	1593	32	1345	78	3	0.61
Graphite[a]	1582					

[a]Reference 4.

higher temperature range ($T>10$ K) and shows a slight drop in the lower temperature region ($T<10$ K) like that for HTT380. The χT vs T plots for the Br-ZTC and HTT780 samples are almost temperature-independent in the higher temperature range ($T>10$ K) and show a slight drop in the lower temperature region ($T<10$ K), similar to the case of HTT380. However, the absolute value of χT for Br-ZTC and HTT780 is almost half that in the case of HTT380. Table II summarizes the temperature-independent diamagnetism terms for all the samples.

The magnetization curves for the HTT380 sample at 2 K and those for K-ZTC at 2, 16, and 30 K are shown in Fig. 8 with the Brillouin curve $S=1/2$, where the spin concentration for calculating the Brillouin curve was obtained by using the Curie constant for HTT380 with assumption of the spin quantum number of $S=1/2$ for the edge-state spin on the basis of the theoretical results.[14]

For the HTT380 sample, the magnetization, which shows localized spin magnetism without hysteresis, is lower than that expected from the noninteracting spins (Brillouin curve $S=1/2$)

The magnetization curve for K-ZTC shows weak hysteresis at 2 K in the intermediate field range between 1 and 4 T, although the magnetization value is almost equal to that for HTT380. The hysteresis becomes almost non-noticeable at temperatures above 16 K.

The ESR signal is described by a single Lorentzian line for all the samples. Figure 9 shows the temperature-dependence of the ESR intensity and the linewidth for the HTT380 and K-ZTC samples. In both samples, the intensity shows Curie-type behavior in the high-temperature region above ca. 20 K, but the intensity is gradually suppressed and starts decreasing below 20 K. At room temperature, the linewidth for the HTT380 sample is around 0.06 mT and is almost temperature-independent, while that for the K-ZTC is 0.11 mT at room temperature and decreases with decreasing temperature. This decrease in the linewidth is gradually suppressed around 20 K. The minimum linewidth is attained at 16 K, and subsequently, the linewidth rapidly increases as the temperature decreases.

TABLE II. The temperature independent terms of the magnetic susceptibility for non-HT, HTT200, HTT300, HTT380, K-ZTC, and Br-ZTC.

Sample	χ_0/emu $g^{-1} \times 10^{-6}$
non-HT	−0.6
HTT200	−0.7
HTT300	−0.6
HTT380	−0.6
HTT780	−0.4
K-ZTC	−0.4
Br-ZTC	−0.2

IV. DISCUSSION

A. Structural change during pretreatment and guest adsorption

In the ambient condition, the ZTC sample contains a large concentration of foreign chemical species, which signifi-

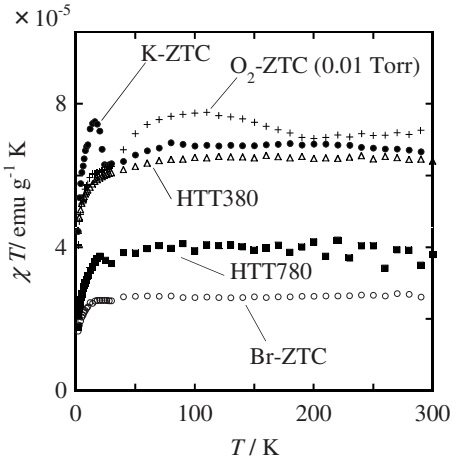

FIG. 7. The temperature-dependence of the χT value for nonadsorbed ZTC (HTT380), HTT780, Br-ZTC, K-ZTC, and O_2-ZTC (0.01 Torr). The open triangles, squares, open circles, closed circles, and crosses represent ZTC (HTT380), ZTC (HTT780), Br-ZTC, K-ZTC, and O_2-ZTC (0.01 Torr), respectively. Each datum is obtained after the temperature-independent term is subtracted from the observed susceptibility.

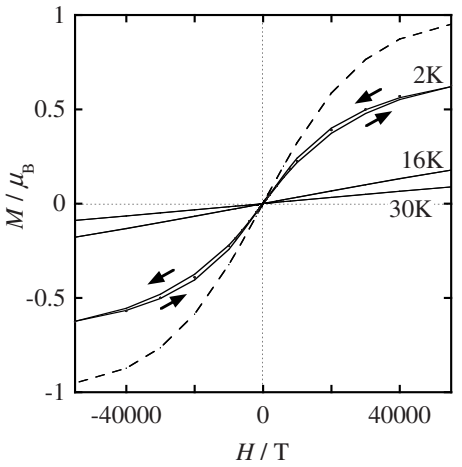

FIG. 8. The magnetization curves for nonadsorbed ZTC (HTT380) at 2 K and K-ZTC at 2, 16, and 30 K. The solid lines represent the curves for K-ZTC at 2, 16, and 30 K, while small closed circles represent the curve for ZTC (HTT380). The arrows represent the direction of the field sweep. The dashed line represents the Brillouin curve of noninteracting spins ($S=1/2$) at 2 K.

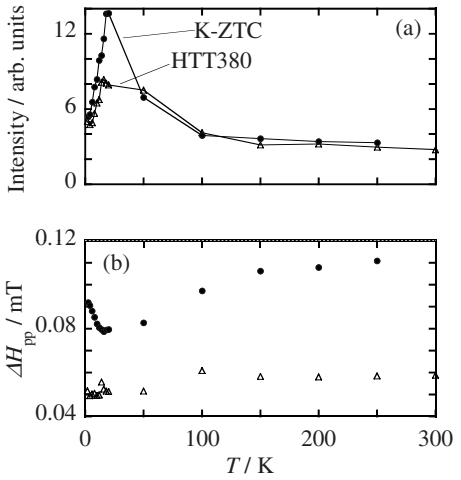

FIG. 9. The temperature-dependence of the ESR intensity (a) and ESR linewidth (b) for the nonadsorbed ZTC (HTT380) (open triangles) and K-ZTC (closed circles).

cantly modify its magnetic properties because of its very large specific surface area ($\sim$3000 $m^2\,g^{-1}$).[28] Thus, such chemical species should be removed from the sample prior to measurements by degassing it at a high temperature in vacuum. However, there is a possibility that the heat-treatment process in vacuum at high temperatures damages the structure of ZTC. The guest adsorption process can also be harmful to the host ZTC structure. In order to investigate the details of the host-guest interaction, it is important to carefully evaluate the stability of the host material structure. Thus, the stability of vacuum-heat-treated and guest-adsorbed ZTC samples was first investigated by structural analysis.

Prior to the investigation of the effect of vacuum-heat-treatment or guest adsorption, the stability of the 3D curved graphene network structure of the as-prepared ZTC was examined. The sharp peak around 6.5° appearing in the XRD profiles for the non-HT samples proves the presence of a periodic structure with a periodicity of 1.4 nm. Indeed, it matches the periodicity of the networked cages of the zeolite Y template rather than that of the graphene honeycomb or sheet stacking structure. The periodicity of 1.4 nm is therefore attributed to the 3D network in the ZTC structure. In addition, the absence of the XRD peak for graphite (002) suggests that the graphene sheets in ZTC are not stacked. This suggests that the arrayed nanopore structure of the zeolite template is transcribed into the graphene network of ZTC.

The results of Raman spectroscopy reveal specific features of the graphene honeycomb structure of ZTC. The emergence of the G and D bands in the Raman spectrum means the presence of the graphene structure; the G band and the D band correspond to the vibrational modes assigned to the π-conjugated bonding and ringed sp^2-carbon structure, respectively. The ratio of the G band and D band intensities, I_G/I_D, provides information on the degree of the spatial extent of the graphene honeycomb network. By applying the empirical formula for graphitic carbon materials,[32] the size of the graphene sheet is estimated as 2–3 nm for the non-HT sample (see Table I). Here, the coefficient in the formula is corrected with respect to the excitation-energy dependence.[33] Since the diameter of the supercage of zeolite Y (1.3 nm) is smaller than the size of the graphene sheet, the graphene sheet having a size of 2–3 nm cannot exist as a flat sheet but must exist as a curved sheet along the wall of the supercage of the zeolite template in ZTC.

Next, the effect of vacuum heat-treatment on the structure of ZTC was investigated. The structural change in the 3D network of the arrayed nanopores during heat-treatment is well characterized by the XRD results. As shown in Fig. 3, the periodic structure of the arrayed nanopores was preserved even after the vacuum-heat treatment up to 380 °C. This implies that the thermal decomposition of the functional groups at the edge part of graphene sheets, as indicated by the TDS results, does not destroy the fundamental graphene backbone of the ZTC structure during the vacuum-degassing process up to 380 °C.

The Raman spectra also support the thermal-proof nature of the ZTC network structure. The common features of the spectra for non-HT, HTT200, HTT300, and HTT380 indicates the robustness of the backbone structure of ZTC to the heat treatment up to 380 °C. On the other hand, the line shape for HTT780 is clearly different from that of other samples. The increase in the linewidth and the downward shift of the G-peak position for HTT780 (see Table I) indicate the destruction of the ZTC graphene backbone. The G-band peak position for HTT780 is much closer to that for graphite, suggesting that the curved graphene structure relaxes into a thermodynamically stable flat graphene structure. This local structural modification induces successive disappearance of the periodicity of the 3D graphene network. This is indicated by the fact that the peak around 6.5° in the XRD profile is gradually suppressed with an increase in the heat-treatment temperature above 380 °C, and completely vanishes at 780 °C.[34]

Here, it should be mentioned that the G-band position (1610 cm^{-1}) is significantly higher than that in the case of

graphite (1582 cm^{-1}) (Ref. 4) for non-HT, HTT200, HTT300, HTT380 (see Table I). In the graphene structure, the *G*-band position is generally related to the occupation of the π band through strong electron-phonon coupling, where electrons (holes) partially occupying the bottom (top) of the antibonding (bonding) π^*-(π-) band cause softening (hardening) of the C–C bonds. The TDS results indicate that the non-HT sample has oxygen-contained functional groups, whose concentration is estimated as 8.9% on the basis of recent results.[25] Thus, charge transfer from the graphene backbone to the oxygen sites of the functional groups on the edges can contribute to hole doping and the upward shift of the *G*-band peak. However, even in the case of the sample heat-treated at 380 °C, which is determined to have a low oxygen concentration on the basis of TDS results, the *G* band still remains at the higher position. The observed upward shift therefore cannot be explained by the charge transfer; the mechanism of this shift is different. A recent theoretical study reveals the hardening of the *G* mode for SWNT through the enhancement of the electron-phonon coupling, when the graphene structure is curved.[35] This allows us to conclude that the curved nature of graphene sheet is the reason for the observed upward shift of the *G* band; nonetheless, a small contribution of charge transfer cannot be ignored, taking into account the slight upward shift observed in HTT780 with respect to graphite. The minor thermally stable oxygen-containing functional groups, which survive even after the heat-treatment up to 780 °C, are responsible for the slight charge transfer.

Let us discuss the effect of the guest adsorption on the ZTC structure. As shown in Fig. 3, the x-ray diffraction peak around 6.5° corresponding to the 3D periodic nanopore network of ZTC is preserved during the potassium adsorption process. The line shape of the Raman spectrum for K-ZTC shown in Fig. 5 resembles that for the HTT380 sample, except for the downward shift in the *G*-band peak (from 1610 cm^{-1} to 1601 cm^{-1}). The observed XRD and Raman spectroscopy results for the K-ZTC sample suggest that the ZTC backbone structure does not collapse during the potassium adsorption process. Moreover, the downward shift of the Raman *G* band upon potassium uptake is understood by considering the occupation of the π-band via charge transfer from the guest potassium, which is a strong electron donor. Empirically, the doping-induced peak shift Δk (cm^{-1}) of the *G* band in graphene is related to the rate f_c of charge transfer per carbon atom from graphene to guest species according to the relation;[36,37] $-1.63\times10^{-6}(\Delta k)^2=0.157f_c+0.146f_c^{3/2}+0.236f_c^2$. Using this relation with $\Delta k=1601-1610$, the charge transfer rate f_c is estimated as $f_c=1-2\times10^{-3}$ for K-ZTC, which is more than two orders of magnitude smaller than that for bulk potassium intercalated graphite ($f_c=0.075$ for KC_8).[5] This extremely small charge transfer can be explained by the structural features of the ZTC, which consists of an arrayed nanopore network of nonstacked single sheets of curved nanographene. First, because of the absence of stacking structures, chemically active graphitic galleries into which potassium atoms are intercalated for charge transfer in the case of graphite intercalation compounds cannot be obtained. Instead, the adsorbed potassium atoms are accommodated into the nanospace surrounded by the curved graphene wall and form nanoclusters in ZTC, where a loosely bounded structure is responsible for the weak interaction between the adsorbed potassium and graphene. In addition, and more importantly, we have to take into account the fact that the amphoteric nature of graphene is degraded in the curved structure of the nanographene sheet. Indeed, the curvature causes the mixing of sp^3 character in the p_z-electronic state, resulting in a lower density of states or the creation of a gap at the Fermi energy in the ZTC host. This negatively affects the charge transfer, as evident from the extremely small charge transfer rate.

Regarding the Raman spectra, it should be noted that the linewidth of the *G* band for K-ZTC is reduced compared to that for HTT380. In general, the broadening of the Raman peak occurs in the case of structural damage because of the random potential and structural disorder. In the case of the HTT780, where the curved graphene structure is destroyed, the downward shift of the *G* band is accompanied by linewidth broadening. Meanwhile, it is known that the *G*-band shift induced by charge transfer in the curved graphene is accompanied by linewidth narrowing;[38] here, the shift of the Fermi energy by doping suppresses the phonon annihilations into an electron-hole pair through the Kohn anomaly effect. This contributes significantly to the homogeneous broadening of the *G*-band peak. It follows that the linewidth narrowing followed by the downward shift in the *G* band of the K-ZTC is a consequence of the charge transfer from potassium; the curved structure of the graphene in the ZTC structure is preserved during potassium adsorption unlike the case for HTT780.

In contrast to K-ZTC, the ZTC structure is drastically modified in the case of bromine adsorption, as indicated by the disappearance of the fingerprint diffraction peak (6.5°) of the ZTC superstructure. The Raman spectrum for Br-ZTC is different from that for HTT380 and resembles that for HTT780, where the ZTC backbone structure is destroyed. The bromine adsorption results in the downward shift of the *G*-band accompanied by an increase in the linewidth (Table I). These experimental results demonstrate that the graphene sheet becomes flat after the curved graphene network of ZTC is completely destroyed in Br-ZTC. Here, it should be noted that the occurrence of a slight shift in Br-ZTC with respect to graphite is given by $f_c=1-2\times10^{-3}$, which is similar to that for K-ZTC, and it indicates that the charge transfer between ZTC and bromine, as well as that between K-ZTC and graphene, is quite weak. Remember that a similar charge transfer indicated by the slight Raman shift with respect to graphite occurs in the case of HTT780; this is caused by thermally stable minor oxygen-containing functional groups bonded to the graphene edges. Eventually, the bromine adsorbed in the nanopores slightly contributes to the charge transfer; the extent of this charge transfer is similar to that induced by the oxygen-containing functional groups.

We can summarize the effect of heat-treatment and guest adsorption as follows: The ZTC structure can be preserved in the heat-treatment below 380 °C or potassium adsorption, whereas it is destroyed above this temperature or during bromine adsorption. The destructive feature of bromine adsorption will be discussed later in relation to the origin of the localized spins.

B. Magnetic properties of ZTC

As mentioned in the introduction, the ferromagnetic features of the as-prepared ZTC (non-HT) have been previously reported.[26] According to the reported study, a ferromagnetic transition occurs at 30 K. This is accompanied by slight spontaneous magnetization created below the Curie temperature. However, the details of the sample characterizations and the measurements are not provided. In the present study, no ferromagnetism is detected in the nonadsorbed ZTC (non-HT, HTT200, HTT300, HTT380), although we confirmed the reproducibility of the experiment many times. As we report here, the magnetism of ZTC is sensitive to the atmosphere and sample treatment conditions. Such strong dependency of magnetism on the sample is understood by considering the nanoporous nature and the presence of chemically active site, namely, the curved part and the edge of graphene. Therefore, without detailed characterization of the sample, we cannot conclude the presence of the ferromagnetism of the nonadsorbed ZTC.

First, we discuss the magnetic properties of ZTC in relation to the heat-treatment effect. In the present study, the non-HT sample and the samples heat-treated up to 380 °C show paramagnetic behavior over the entire range of measurement temperatures (2–300 K), as seen in the static susceptibility (Fig. 6). The ESR intensity (Fig. 9) shows an apparent decrease, indicating a magnetic transition in the lowest temperature region. However, this apparent decrease is a consequence of the saturation effect because of the high microwave power in this experiment (1 mW).[39] In addition, a hump appears in the χT plot for the non-HT and HTT200 samples. The hump corresponds to the magnetism of the adsorbed oxygen molecules included in the ambient gases, as this generally appears in the porous materials. Indeed, a similar hump appears in the sample that was intentionally contaminated by a small amount of oxygen [O_2-ZTC (0.01 Torr)], as shown in Fig. 7. The suppression of the hump upon a further increase in the heat-treatment temperature indicates the successful degassing of the adsorbed oxygen molecules. The oxygen content becomes lower than the detection level in the magnetic measurements for HTT300 and HTT380. In this case, TDS results reveal that the thermally unstable functional groups at the edge sites of curved graphene are also decomposed. On the other hand, the magnetic susceptibility for HTT780 changes significantly and its absolute value decreases considerably relative to the corresponding values for non-HT, HTT200, HTT300, and HTT380. This is consistent with the fact that the ZTC structure is destroyed in the HTT780 sample, and the magnetism of the HTT780 sample is very different from the intrinsic magnetism of ZTC. Thus, in the following discussion, we mainly focus on the sample vacuum-heat-treated at 380 °C (HTT380) as nonadsorbed ZTC.

The magnetic susceptibility for the nonadsorbed ZTC (HTT380) is expressed in terms of the Curie-Weiss term χ_C and the temperature-independent term χ_0. The temperature-independent term is obtained as -0.6×10^{-6} emu g^{-1} by extrapolating the susceptibility to infinite temperature. The absolute value of χ_0 for HTT380 is smaller than that in the case of flat nanographene with an in-plane size of 2–3 nm ($-0.8\sim-0.9\times10^{-6}$ emu g^{-1}) in ACFs (Refs. 6 and 7) but larger than that in the case of diamond (-0.5×10^{-6} emu g^{-1}). The value of χ_0 for diamond is well explained by the Pascal core diamagnetism. The larger absolute value of χ_0 for nanographene is attributed to the contribution of the orbital magnetism of the π electron. The strength of the orbital susceptibility represents the extent of the π-conjugate system in carbon materials. The observed absolute value (-0.6×10^{-6} emu g^{-1}), which is smaller than that of nanographene in ACFs, indicates that ZTC has a graphitic π-electron network whose extent is smaller than that of the nanographene sheet in ACFs. This is caused by the nonflat graphene structure, in which the sp^3 nature is admixed with the π-electron state. The absolute value of χ_0 in HTT780 (-0.4×10^{-6} emu g^{-1}) is slightly less than that for HTT380, being consistent with the defective nature caused by the destruction of the curved structure of graphene sheet in HTT780. The disorder in the graphene sheet structure, which is evidenced by the large linewidth of the *G*-band peak in the Raman spectrum, gives the smaller extent of the π-conjugate system in HTT780.

Let us investigate the detailed behavior of the localized spins on the basis of the experimental results. From the Curie-Weiss term χ_C, the localized spin density is found to be 1×10^{20} g^{-1} for HTT380. The reduction in χT, which represents the effective magnetic moment, below 10 K indicates the presence of weak antiferromagnetic interaction between localized spins. This is also indicated by the small negative Weiss temperature (less than 1 K). From the spin density and mass density of ZTC (1.63 cm^{-3} g), the latter of which is calculated by using the structural model based on the geometry of the pore for Y-zeolite, the average inter-spin distance is estimated as 1.8 nm; the estimation is based on the assumption of the homogeneous spatial distribution of the spins in average. The obtained average inter-spin distance roughly matches the periodicity of ZTC (1.4 nm). Thus, we can conclude that each structural unit of the ZTC porous network has a single spin.

The following discussion is devoted to the origin of the localized spins present in ZTC. In amorphous carbon materials, the unpaired electrons belonging to the dangling bonds are attributed to the origin of the localized spin. However, in the case of nanoporous carbon materials like ZTC, where σ-dangling bonds are completely exposed to the ambient atmosphere, the dangling bonds are immediately terminated because of foreign species such as oxygen molecules in the ambient environment. Therefore, the dangling bond spins cannot be classified as the localized spins observed in ZTC. The present experimental result that the spin concentration is independent of the heat-treatment temperature suggests that the functional groups are not responsible for the localized spins, because the heat-treatment decomposes the functional groups as indicated by the TDS results. Instead, we should remember that ZTC consists of a combination of cup-like curved graphene and the thinner cullislike curved graphene, where the edge-state spin and radical spin of negative curved graphene exist at the graphene edges and the crotch-shaped part between the cup and cullis, respectively, in the curved graphene network. The localized spins of the nonbonding π-edge states can survive in the presence of the chemically

active foreign species. The radical spins of the unpaired electrons of undercoordinated carbon atoms are also relatively inert as they are sterically stabilized by surrounding sp^2 carbon atoms in the strained saddle parts of the negatively curved graphene network. This is similar to the case of radical molecules stabilized by bulky functional groups whose steric effect protects the radical state against the attack by chemically active foreign species in the environment.[40] We can conclude that the edge-state spins and the spins in the negatively curved graphene are the origin of the observed spin magnetism in ZTC. This is supported by the change in the magnetism that accompanies the heat-treatment at 780 °C and bromine uptake; in particular, a reduction by half occurring in the spin concentration in HTT780 and Br-ZTC (see Fig. 7), in which the negatively curved structures relaxed and the graphene edges are not seriously affected. Some localized spins remain in Br-ACFs and HTT780; this indicates the coexistence of the radical spins at the curved part and edge-state spins at the graphene edges.

Here, the highly sensitive nature of the curved graphene structure of ZTC to bromine uptake is discussed. In comparison with the interior carbon site of flat graphene, which is robust to the bromine attack, the carbon site on the geometrically strained network is more sensitive to the reaction with bromine. Therefore, the negatively curved graphene structure is destroyed by the bromine adsorption, following by the approximately 50% reduction in the spin concentration.

C. Magnetic order in potassium adsorbed ZTC

In this section, we discuss the magnetism of potassium clusters accommodated in the nanopore space. The temperature-independent term χ_0 (-0.4×10^{-6} emu g^{-1}) for K-ZTC shows a slight positive shift compared to that for the nonadsorbed ZTC (-0.6×10^{-6} emu g^{-1}). The change in the Fermi energy of ZTC induced by the charge transfer from potassium ($f_c=1-2\times10^{-3}$) is too small to induce a change in the Pauli paramagnetism of ZTC. In fact, it is two orders of magnitude smaller than that for bulk graphite potassium intercalation compounds[5] and less than that in potassium-adsorbed flat nanographene of ACFs.[10] Thus, the slight observed change in χ_0 is attributed partly to magnetism originating from the adsorbed potassium atoms, which form clusters in the nanopore space.

As shown in Fig. 7, χT for K-ZTC exhibits a sharp peak at 16 K; there is no other significant difference between K-ZTC and ZTC (HTT380). This peak is well reproduced for the samples prepared by using the pristine ZTC in various pre-treatment conditions (HTT200, HTT300, and HTT380) and is not attributed to an extrinsic origin. As possible reasons for the appearance of this peak, we note the contaminations of the oxygen molecules and KO_2 during the potassium adsorption process, the latter of which is possibly contained as an impurity in starting potassium even after sufficient purification. KO_2 exhibits an antiferromagnetic transition. Here, a peak feature in the χT value is sometimes observed. However, the transition temperature of KO_2 is 7.1 K,[41] which is clearly lower than the peak temperature of 16 K for K-ZTC. The contamination of the magnetic oxygen molecules is also often suspected to occur during the magnetic measurement. However, in the temperature-dependence plot of χT for O_2–ZTC (0.01 Torr) shown in Fig. 7, as generally seen in oxygen-contaminating porous materials, the χT value shows a broad hump around the temperature range 50–100 K; this hump is different from the peaklike feature appearing around 16 K. The contribution of either oxygen molecules or KO_2 species is therefore excluded. Although the change in the magnetism of ZTC upon potassium uptake should also be considered as another reason for the appearance of the peak, the adsorbed potassium influences the ZTC structure to a lesser extent, and its interactions with the graphene cage are weaker, as discussed in the previous section. The observed ESR linewidth is still sharp and is only doubled upon the adsorption of potassium in ZTC380. If the exchange interaction between the host ZTC and potassium clusters occurs, a large increase in the linewidth in the ESR spectrum is expected for K-ZTC, contradictory to experimental results, since the spin-orbit interaction of potassium is large (38 cm^{-1}).[42,43] It is finally suggested that adsorbed potassium does not influence the magnetism of ZTC. This is also consistent with the fact that the charge transfer interaction between the guest species and host ZTC is quite small. This is because of the mixing in the electronic states between π- and σ state in the curved graphene sheet of ZTC, resulting in the less interaction between ZTC and the guest material. Thus, the χT peak at 16 K is attributed to the magnetism of potassium clusters confined in the nanopores in ZTC.

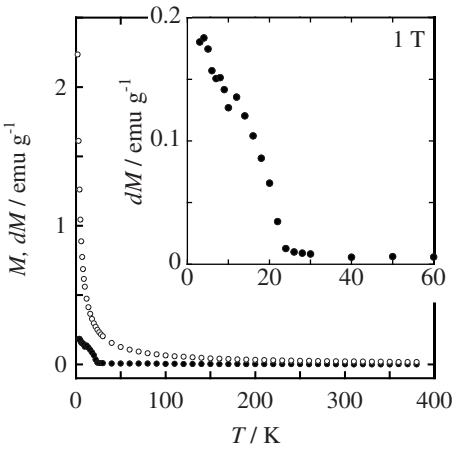

FIG. 10. The temperature-dependence of the magnetization for HTT380 (M: open circles) and the potassium clusters in K-ZTC (dM: closed circles) measured at 1 T. The temperature-independent component is subtracted from each data point. The inset shows a magnified version of the plot of dM in the lower temperature range for K-ZTC.

Let us discuss the magnetism of the spins of the potassium clusters in detail. Because the magnetism of the ZTC is not influenced by potassium adsorption, as seen in the ESR linewidth, the contribution of potassium clusters to the magnetism (dM) is determined by subtracting the magnetization values for ZTC (HTT380) (M) from those for K-ZTC, as shown in Fig. 10. The magnetization exhibits the ordinary Curie-Weiss type temperature-dependence in the high-temperature region ($T>24$ K), while a sharp increase in the

magnetization starts appearing around 24 K. The rapidly increasing magnetization tends to saturate as the lowest temperature is approached. This suggests the onset of ferromagnetic ordering around 24 K. An indication of the ferromagnetism of potassium cluster also appears in the magnetization curves shown in Fig. 8 for the K-ZTC at 2, 16, and 20 K. Here, a hysteretic ferromagnetic contribution of the potassium clusters in K-ZTC is visible in the magnetization at 2 K, on the background of the majority paramagnetic contribution of the spins of curved graphene. As the temperature is increased, the ferromagnetic component becomes unnoticeable above 16 K. Interestingly, the observed remnant magnetization is negligibly small at the zero magnetic fields. Therefore, the small observed hysteresis and remnant magnetization more conclusively suggest the presence of weak ferromagnetism that appears in the range of intermediate field strengths (0.5–4 T).

With respect to the anomalous weak ferromagnetic behavior, we should remember that the potassium cluster confined in the zeolite nanopore shows weak ferromagnetism.[16,17] In the potassium clusters accommodated in a nanopore of zeolite, potassium $4s$ electrons successively occupy the $1s$ and $1p$ states of the super atom (the cluster states). The strong anisotropic interaction between the magnetic moments of adjacent clusters causes a large-angle spin canting with a negative Weiss temperature. This results in the weak ferromagnetic ordered state with a transition temperature of ~ 10 K. The transition temperature is in the same temperature range as the temperature (24 K) at which the magnetization starts increasing in the present experiment. In K-ZTC, the zeolite periodic nanopore network is preserved in the microscopic structure, as discussed above. Thus, the potassium clusters in K-ZTC are arranged in the nanopore network in a manner similar to that in the potassium-doped zeolite systems. Therefore, a similar mechanism might be responsible for the magnetism observed in the potassium clusters in the present system. Interestingly, in comparison with potassium-doped zeolite LTA, K-ZTC has a higher weak ferromagnetic transition temperature (24 K). This is explained by the greater channel width of zeolite Y, which is the template material for the ZTC in the present study. The greater overlap of the wave function of the potassium clusters through the wider channel is a favorable condition for the transition temperature to increase.

For discussing the details, let us assume a magnetic moment similar to the potassium cluster in zeolite, i.e., $0.24\mu_B$ per cluster at 100 Oe and 1.7 K,[16] as the potassium content is not available in the present experiment. Since the excess magnetization below 24 K originates from the spontaneous magnetization in the weak ferromagnetic state of potassium clusters, we can estimate the number of potassium clusters having the spontaneous magnetization from the value of the excess magnetization at $T=0$ K. Then, from the value of the excess magnetization, the number of potassium clusters is estimated as $\sim 1\times 10^{18}/\mathrm{g}$, which is two orders of magnitude smaller than that expected from the nanopore density of ZTC ($\sim 1\times 10^{20}/\mathrm{g}$). This is a reasonable result, since the nanopore network of ZTC does not have a perfectly ordered structure. In other words, the network of the magnetic clusters comprising regular arrays is imperfectly and inhomogeneously formed in K-ZTC, and the volume fraction of the magnetically ordered area is small (0.01) in the present sample.

Interestingly, the ferromagnetic transition of the potassium cluster can be investigated by obtaining the ESR spectrum of the spins of the host ZTC. As seen in the magnetization curves and the ESR linewidth, the magnetism of K-ZTC is governed by that of the host ZTC, and the minority spins in the potassium clusters are not coupled with the spins in ZTC. Namely, the ESR spectrum in K-ZTC is assigned neither to the potassium spins nor to the coupled system of the graphene and potassium spins; rather, it is attributed only to the graphene spins as discussed already. Indeed, using the number and the values of the magnetic moments of the potassium clusters estimated from the magnetization ($0.24\mu_B$ with a density of $1\times 10^{18}/\mathrm{g}$, respectively) and assuming a homogeneous distribution of the moments, the dipolar field of the potassium spins is estimated as 0.07 mT, which is roughly equal to the increase in the observed linewidth upon potassium uptake. Therefore, it is concluded that the spins in the host ZTC are merely affected by the dipolar field of the potassium spins; there is no exchange interaction between the two spin systems. However, as shown in Fig. 9(b), the linewidth for K-ZTC slightly decreases with a decrease in temperature, and this decrease is accompanied by an abrupt increase below 16 K, in contrast to the case of nonadsorbed ZTC. The temperature at which the linewidth begins to broaden is identical to that at which the peak feature appears in the χT plot. The abrupt increase in the linewidth is a consequence of the development of the ferromagnetic internal field in the case of the potassium spins. The development of the magnetic ordering of the potassium cluster spins generates fluctuations in the internal field in K-ZTC. As a result, through the dipolar field, the magnetic ordering of the potassium cluster is reflected in the behavior of the paramagnetic graphene spins of ZTC, which are fundamentally independent of the former.

As already discussed above, the observed ESR signal is assigned to the paramagnetic host spins, which are not subjected to the exchange interaction with potassium spins. Eventually, the abrupt increase in the linewidth is a consequence of the development of the ferromagnetic internal field at the potassium spins. The development of the magnetic ordering of the potassium cluster spins generates fluctuations in the internal field in K-ZTC. As a result, the magnetic ordering of the potassium cluster is mirrored to the behavior of the paramagnetic graphene spins of ZTC, which are independent from the former.

Finally, we comment on the difference between the behavior observed in the present results and that of the ACFs consisting of flat nanographene sheets.[10] In the latter case, potassium antiferromagnetic clusters created in the ACF nanopores interact more strongly with flat nanographene sheets than they do with the curved graphene sheets in the present case. The curvature in the graphene sheets plays an important role in producing the weak ferromagnetic feature similar to that in the potassium cluster in zeolite and dissimilar to the magnetism of the potassium cluster in ACFs.

V. CONCLUSION

The curved graphene network with the regularly aligned array of nanopores is investigated from the viewpoints of structure and magnetism, and its guest adsorption effect by using zeolite-templated carbon (ZTC), which is composed of the curved graphene cups that form nanopores with a diameter of ~1 nm and are connected by the graphene cullis with a diamond network structure. The ZTC structure is preserved during both heat-treatment up to 380 °C under vacuum and potassium adsorption, in spite of the destructive effect of heat-treatment up to 780 °C and bromine adsorption. The presence of curvature, as well as an edge, in graphene generates localized magnetism. In particular, the edge-state spins at the edge and radical spins at the regions of negative curvature of the graphene network generate the localized spins, resulting in paramagnetism for nonadsorbed ZTC at all measurement temperatures down to 2 K. In the case of potassium adsorption, potassium atoms are accommodated as clusters in the nanopores in ZTC without significant electronic interaction with the curved graphene host. Potassium clusters in the nanopore network in ZTC exhibit weak ferromagnetic ordering around 24 K; here, a spin canting is responsible for the weak ferromagnetism. The localized spins of the ZTC host system, which are well isolated from the potassium guest, can act as an accurate probe for the detection of the magnetism of guest species.

ACKNOWLEDGMENTS

The present work was supported by the Grant-in-aid for Scientific Research Grant No. 19051006 and Grant No. 20001006 from Ministry of Education, Culture, Sports, Science and Technology.

*ktakai@chem.titech.ac.jp

[1] S. Kitagawa, R. Kitaura, and S. Noro, Angew. Chem., Int. Ed. **43**, 2334 (2004).
[2] Proceedings of the 5th International Meeting on Small Particles and Inorganic Clusters, edited by O. Echt and E. Rechnagel (Springer International, Berlin, 1991).
[3] S. Sugano, *Microcluster Physics* (Springer-Verlag, Berlin, 1991).
[4] M. S. Dresselhaus, G. Dresselhaus, and P. C. Eklund, *Science of Fullerenes and Carbon Nanotubes* (Academic Press, San Diego, 1996).
[5] T. Enoki, M. Suzuki, and M. Endo, *Graphite Intercalation Compounds and Applications* (Oxford University Press, New York, 2003).
[6] T. Enoki and K. Takai, Dalton Trans. **2008**, 3773.
[7] T. Enoki and K. Takai, in *Carbon-Based Magnetism*, edited by F. Palacio and T. Makarova (Elsevier, Amsterdam, 2006), pp. 397–416.
[8] Y. Shibayama, H. Sato, T. Enoki, Xiang-Xin Bi, M. S. Dresselhaus, and M. Endo, J. Phys. Soc. Jpn. **69**, 754 (2000).
[9] K. Takai, H. Kumagai, H. Sato, and T. Enoki, Phys. Rev. B **73**, 035435 (2006).
[10] K. Takai, S. Eto, M. Inaguma, T. Enoki, H. Ogata, M. Tokita, and J. Watanabe, Phys. Rev. Lett. **98**, 017203 (2007).
[11] K. Takahara, K. Takai, T. Enoki, and K. Sugihara, Phys. Rev. B **76**, 035442 (2007).
[12] K. Takai, H. Sato, T. Enoki, N. Yoshida, F. Okino, H. Touhara, and M. Endo, J. Phys. Soc. Jpn. **70**, 175 (2001).
[13] K. Tanaka, S. Yamashita, H. Yamabe, and T. Yamabe, Synth. Met. **17**, 143 (1987).
[14] M. Fujita, K. Wkabayashi, K. Nakada, and K. Kusakabe, J. Phys. Soc. Jpn. **65**, 1920 (1996).
[15] M. Fujita, M. Igami, and K. Nakada, J. Phys. Soc. Jpn. **66**, 1864 (1997).
[16] Y. Nozue, T. Kodaira, and T. Goto, Phys. Rev. Lett. **68**, 3789 (1992).
[17] R. Arita, T. Miyake, T. Kotani, M. van Schilfgaarde, T. Oka, K. Kuroki, Y. Nozue, and H. Aoki, Phys. Rev. B **69**, 195106 (2004).
[18] T. Kyotani, T. Nagai, S. Inoue, and A. Tomita, Chem. Mater. **9**, 609 (1997).
[19] A. L. Mackay and H. Terrones, Nature (London) **352**, 762 (1991).
[20] M. Fujita, T. Umeda, and M. Yoshida, Phys. Rev. B **51**, 13778 (1995).
[21] M. Ikegami and Y. Nagaoka, Prog. Theor. Phys. Suppl. **106**, 235 (1991).
[22] H. Aoki, M. Koshino, D. Takeda, H. Morise, and K. Kuroki, Phys. Rev. B **65**, 035102 (2001).
[23] M. Koshino and H. Aoki, Phys. Rev. B **71**, 073405 (2005).
[24] N. Park, M. Yoon, S. Berber, J. Ihm, E. Osawa, and David Toma'nek, Phys. Rev. Lett. **91**, 237204 (2003).
[25] H. Nishihara, Q. H. Yang, P. X. Houa, M. Unnoa, S. Yamauchi, R. Saito, J. I. Paredesd, A. Marti'nez-Alonsod, J. M. D. TascoLnd, Y. Sato, M. Terauchi, T. Kyotani, Carbon. **47**, 1220 (2009).
[26] Y. Kopelevich, R. R. da Silva, J. H. S. Torres, A. Penicaud, and T. Kyotani, Phys. Rev. B **68**, 092408 (2003).
[27] X. Ma, T. Kyotani, Z. Liu, O. Terasaki, and A. Tomita, Chem. Mater. **13**, 4413 (2001).
[28] P. Hou, T. Yamazaki, H. Orikasa, and T. Kyotani, Carbon **43**, 2624 (2005).
[29] Y. Otake and R. G. Jenkins, Carbon **31**, 109 (1993).
[30] Q. L. Zhuang, T. Kyotani, and A. Tomita, Carbon **32**, 539 (1994).
[31] U. Zielke, K. J. Huttinger, and W. P. Hoffman, Carbon **34**, 983 (1996).
[32] D. S. Knight and W. B. White, J. Mater. Res. **4**, 385 (1989).
[33] L. G. Cancado, K. Takai, T. Enoki, M. Endo, Y. A. Kim, H. Mizusaki, A. Jorio, L. N. Coelho, R. Magalhaes-Paniago, and M. A. Pimenta, Appl. Phys. Lett. **88**, 163106 (2006).
[34] T. Yamazaki, Mater thesis, Tohoku University, 2004.
[35] K. I. Sasaki, R. Saito, G. Dresselhaus, M. S. Dresselhaus, H. Farhat, and J. Kong, Phys. Rev. B **77**, 245441 (2008).
[36] L. Pietronero and S. Strässler, Phys. Rev. Lett. **47**, 593 (1981).
[37] C. T. Chan, K. M. Ho, and W. A. Kamitakahara, Phys. Rev. B **36**, 3499 (1987).

[38] H. Farhat H. Son, Ge. G. Samsonidze, S. Reich, M. S. Dresselhaus, and J. Kong, Phys. Rev. Lett. **99**, 145506 (2007).
[39] K. Takai, T. Suzuki, T. Enoki, H. Nishihara, and T. Kyotani, J. Phys. Chem. Solids **71**, 565 (2010).
[40] M. Gomberg, J. Am. Chem. Soc. **22**, 757 (1900).
[41] M. Labhart, D. Raoux, W. Känzig, and M. A. Bösch, Phys. Rev. B **20**, 53 (1979).
[42] B. A. Goodman and J. B. Raynor, in *Adv. Inorg. Chem. and Radio Chem.*, edited by H. J. Emeleus and A. G. Sharpe (Academic Press, New York, 1970), Vol. 13.
[43] J. A. McMillan and T. Halpern, Based upon the wave functions of Charlotte Froese, *Hartree-Fock Parameters for the Atoms Helium to Radon*, Dept. Math., Univ., British Columbia (1966).